RADIO SCIENCE, VOL. 45, RS1008, doi:10.1029/2008RS003989, 2010

Reducing the effects of noise on atmospheric imaging radars using multilag correlation

K. D. Le,[1,2] R. D. Palmer,[1,3] B. L. Cheong,[1] T.-Y. Yu,[1,2] G. Zhang,[1,3] and S. M. Torres[1,4]

Received 7 August 2008; revised 11 July 2009; accepted 8 October 2009; published 4 February 2010.

[1] Atmospheric imaging radars offer the capability to scrutinize structures within the illuminated volume at high temporal and spatial resolutions. The retrieval of the mean signal power using an imaging radar is obtained by subtracting the noise power from the covariance function at lag zero. The results obtained at low signal-to-noise ratio (SNR) are problematic when the noise power is unsuccessfully estimated, and are difficult to interpret when adaptive weights are used because of the temporally varying noise power. In this paper, a processing technique that improves the retrieval of the mean signal power by exploiting the temporal correlation difference between the desired signal and system noise is presented. Simulations of its performance are presented for the special case of a Gaussian received spectrum for variations in SNR, normalized spectrum width, and number of time series samples. The technique is also applied to real data collected with the Turbulent Eddy Profiler, a vertically pointing phased array radar developed at the University of Massachusetts, between 1435 and 1457 UTC 15 June 2003. Even though the performance of this technique in terms of its variance and bias depends on the SNR, spectrum width, and number of time series samples, results from both simulations and real data are promising as an enhanced mean signal power in the low SNR regions is obtained.

Citation: Le, K. D., R. D. Palmer, B. L. Cheong, T.-Y. Yu, G. Zhang, and S. M. Torres (2010), Reducing the effects of noise on atmospheric imaging radars using multilag correlation, *Radio Sci.*, *45*, RS1008, doi:10.1029/2008RS003989.

1. Introduction

[2] The quality of atmospheric radar observations is limited by slow update times, clutter contamination, and range velocity ambiguities, among other factors [*Battan*, 1973; *National Research Council*, 2002; *Doviak and Zrnić*, 1993; *Friedrich et al.*, 2006]. Imaging radars consist of a widebeam transmitter and many independent receiving subarrays, and can mitigate some of these problems by illuminating a large field of view and using adaptive beamforming to scrutinize the structures and dynamics within this region. These radars have been applied to investigate clear-air turbulence and precipitation [*Mead et al.*, 1998; *Palmer et al.*, 1993, 2005], plasma irregularities in the equatorial *F* region [*Hysell*, 1996], structures of the polar mesosphere summer echoes [*Yu et al.*, 2001], airborne clutter sources in the boundary layer [*Cheong et al.*, 2006], and phenomena in the stratosphere-troposphere (ST) layers [*Hélal et al.*, 2009], among others [*Fukao*, 2007].

[3] Currently, the observation of mean signal power using an imaging radar is typically obtained by subtracting the noise power from the covariance function at lag zero. Classic techniques used in obtaining the mean signal power include signal statistics separation [*Hildebrand and Sekhon*, 1974], spectral thresholding [*Gordon*, 1997], spurious spectral peaks averaging [*Marple*, 1987], and matched filters [*Haykin*, 1996]. The mean signal power is unfortunately biased if the noise power is unsuccessfully estimated. A natural incentive exists to obtain the signal power in a way that bypasses the need for estimating the noise power. In this paper, a multilag (ML) correlation technique is introduced that satisfies this requirement by exploiting the temporal correlation difference between the scattered atmospheric signal and the receiver noise. Previously, higher-order correlation values have been used for similar purposes to retrieve velocity [*Strauch*

[1]Atmospheric Radar Research Center, University of Oklahoma, Norman, Oklahoma, USA.
[2]School of Electrical and Computer Engineering, University of Oklahoma, Norman, Oklahoma, USA.
[3]School of Meteorology, University of Oklahoma, Norman, Oklahoma, USA.
[4]Cooperative Institute for Mesoscale Meteorological Studies, University of Oklahoma, Norman, Oklahoma, USA.

0048-6604/10/2008RS003989$11.00

et al., 1978], spectrum width [*Srivastava and Jameson*, 1979], linear depolarization ratio [*Melnikov*, 2006; *Hubbert et al.*, 2003], and cross-polarization ratio [*Melnikov*, 2006].

[4] In the next section, the derivation of the ML technique and simulation of its performance for a Gaussian spectrum time series signal are presented. In section 3, the ML technique is applied to real data and the results are compared to those obtained using conventional Fourier and adaptive Capon beamforming. In section 4, conclusions are presented.

2. Theoretical Foundation

[5] Time series signals measured at the individual array elements are mathematically represented using the array model of *Stoica and Moses* [2005]. It is described using an array transfer function, a narrowband signal that simulates the scattered signal, and additive receiver noise. The ML technique is then derived, and a specific example of the ML technique for lag 1 and 2 is introduced. The performance of the ML technique for lag 1 and 2 is then investigated via simulations for variations in SNR, normalized spectrum width σ_{vn}, and number of time series samples.

2.1. Array Model and Derivation of Proposed Technique

[6] The vector of time series signals at the subarrays $\{\mathbf{x}(nT_s);\ n = 0, 1, \cdots, N-1\}$, sampled at T_s, is given by the vector

$$\mathbf{x}(nT_s) = \mathbf{A}\mathbf{s}(nT_s) + \mathbf{n}(nT_s), \tag{1}$$

where the array transfer matrix that characterizes the propagation and receiver effects is $\mathbf{A} = [\mathbf{a}(\theta_1)\ \mathbf{a}(\theta_2)\ \cdots\ \mathbf{a}(\theta_d)]$, d is the number of scattering sources, $\mathbf{a}(\theta)$ is the array response vector, $\mathbf{s}(nT_s)$ is the vector of random processes that represent the base band time series of the scattered signal, and $\mathbf{n}(nT_s)$ is the vector of receiver noise. The length of $\mathbf{x}(nT_S)$ is the number of subarray elements.

[7] By a linear combination of the subarray signals, the output signal of the beamformer is given by

$$y(nT_s) = \mathbf{w}^H\mathbf{x}(nT_s), \tag{2}$$

where $(\cdot)^H$ denotes the Hermitian operator. The weights $\mathbf{w}$ are generally selected to be optimal in some sense [*Capon*, 1969; *Harris*, 1978; *Marple*, 1987; *Haykin*, 1996; *Stoica and Moses*, 2005]. Physical and dynamic properties of the scatterers within the imaged volume are then inferred by evaluating the autocorrelation function $R_y(mT_s) = E\{y(nTs)y^*((n-m)T_s)\}$ at different temporal lags, mT_s.

[8] The measured power, P, is obtained by evaluating the correlation at zero lag $R_y(0)$,

$$\begin{aligned} P &= E\{y(nT_s)y^*(nT_s)\} \\ &= \mathbf{w}^H E\{\mathbf{x}(nT_s)\mathbf{x}^H(nT_s)\}\mathbf{w} \\ &= \mathbf{w}^H\left(\mathbf{A}\mathbf{R}_s(0)\mathbf{A}^H + N\mathbf{I}\right)\mathbf{w} \\ &= S + N\mathbf{w}^H\mathbf{w}, \end{aligned} \tag{3}$$

where $\mathbf{R}_s(0) = E\{\mathbf{s}(nT_s)\mathbf{s}^H(nT_s)\}$ and $N\mathbf{I} = E\{\mathbf{n}(nT_s)\mathbf{n}^H(nT_s)\}$. The mean signal power, S, is obtained by subtracting the noise power, $N\mathbf{w}^H\mathbf{w}$, from P. In this derivation, the noise is assumed to be complex Gaussian with zero mean and power N.

[9] In (3), $S = \mathbf{w}^H(\mathbf{A}\mathbf{R}_s(0)\mathbf{A}^H)\mathbf{w}$, which cannot be directly retrieved from P when noise is present. However, by assuming a Gaussian spectrum and using higher-order lags of the covariance function, it is shown in Appendix A (see (A6)) that

$$S = \mathbf{w}^H\left(\mathbf{A}\left(\mathbf{R}_s(mT_s) \otimes \mathbf{C}^{-1}(mT_s)\right)\mathbf{A}^H\right)\mathbf{w}, \tag{4}$$

where $\otimes$ is the Kronecker product and $\mathbf{C}(mT_s)$ is the normalized correlation matrix of the baseband signal between the scatterers. Unfortunately, the spectrum width and Doppler velocity in $\mathbf{C}(mT_s)$ are needed to estimate S.

[10] Using the approximation that the gain in the steered direction is unity and the contribution within the main lobe is dominant, (4) can be reformulated as

$$S \approx \mathbf{w}^H\left(\mathbf{A}\mathbf{R}_s(mT_s)\mathbf{A}^H\right)\mathbf{w}c_{\mathbf{w}}^{-1}(mT_s), \tag{5}$$

where $c_{\mathbf{w}}(mT_s)$ is the element of $\mathbf{C}^{-1}(mT_s)$ in the steered direction. Element $c_{\mathbf{w}}(mT_s)$ can be eliminated by using a ratio of S for different temporal lags. For example, the mean signal power, using temporal lags 1 and 2 (S_{ML}) is given by the following relation

$$\begin{aligned} S_{ML} &\approx \left[\frac{|S|_{m=1}|^4}{|S|_{m=2}|}\right]^{1/3} \\ &= \left(\frac{\left|\mathbf{w}^H\left[\mathbf{A}\mathbf{R}_s(T_s)\mathbf{A}^H\right]\mathbf{w}c_{\mathbf{w}}(T_s)\right|^4}{\left|\mathbf{w}^H\left[\mathbf{A}\mathbf{R}_s(2T_s)\mathbf{A}^H\right]\mathbf{w}c_{\mathbf{w}}(2T_s)\right|}\right)^{1/3}. \end{aligned} \tag{6}$$

Now, $|c_{\mathbf{w}}(T_s)|^4/|c_{\mathbf{w}}(2T_s)| = 1$ if a Gaussian-shaped spectrum is assumed, which is typically for atmospheric scattering. As shown in the work of *Doviak and Zrnić* [1993], the shape of the spectrum of the return signal from

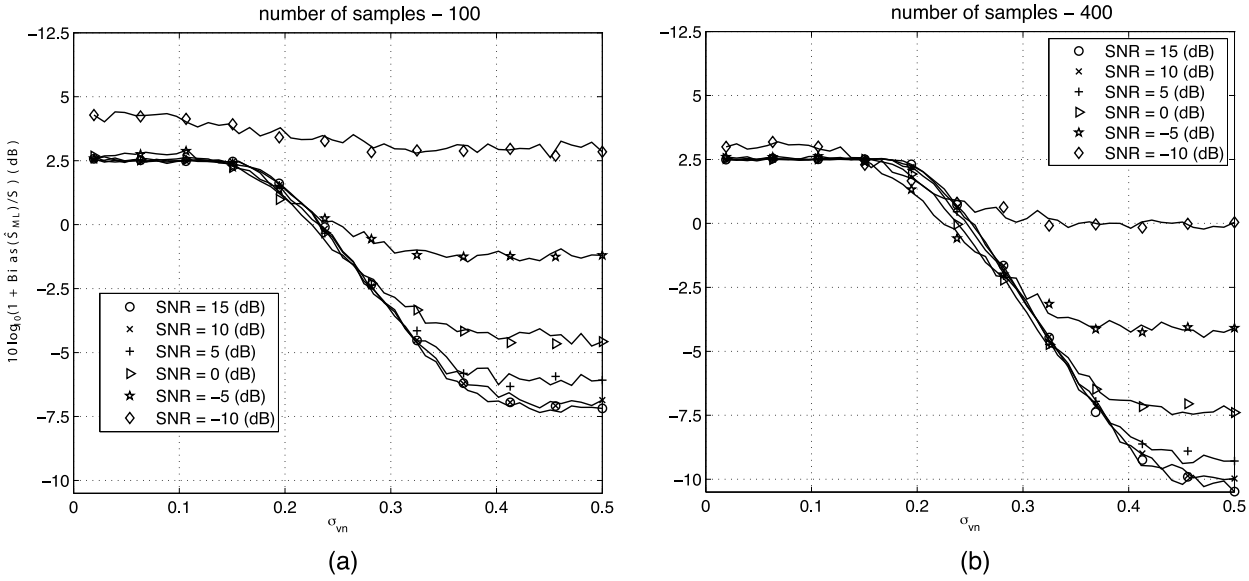

Figure 1. Bias of power estimate obtained using S_{ML} for variation in normalized spectrum width values ($\sigma_{vn} = \sigma/2v_a$). (a) Number of samples − 100. (b) Number of samples − 400. Curves in each plot are generated using 500 realizations and for SNR from −10 to 15 dB at 5 dB intervals at high σ_{vn} resolution. The marked and solid curves are of the same result but are shown for two different resolutions.

a resolution volume encased in a linear wind field is that of the antenna pattern, assuming Taylor's frozen atmosphere hypothesis and long dwell times are applied. Under the above conditions, the mean signal power is

$$S_{ML} \approx \left(\frac{\left| \mathbf{w}^H \left[\mathbf{A} \mathbf{R}_s(T_s) \mathbf{A}^H \right] \mathbf{w} \right|^4}{\left| \mathbf{w}^H \left[\mathbf{A} \mathbf{R}_s(2T_s) \mathbf{A}^H \right] \mathbf{w} \right|} \right)^{1/3}. \qquad (7)$$

Note that this form of S has no component of $c_{\mathbf{w}}(mT_s)$ and, therefore, the radial velocity and spectrum are not needed *a priori*. In addition, the noise power estimated is not needed since lags 1 and 2 are used in the formulation.

2.2. Performance of ML for Gaussian-Shaped Spectra

[11] The nonlinear nature of the ML technique makes it difficult to obtain theoretical information about its statistical behavior. However, a statistical examination using perturbation analysis was made that assumes the measured correlation value can be expressed as its mean and a small zero-mean perturbation. The results, shown in Appendix B, indicate the variance of the two-lag estimator is primarily affected by the SNR, σ_{vn}, and the magnitude and ratio of the two lags that are used in the ML technique. Additionally, the technique performs well only over a limited range of these factors. Outside the selected range, such as at very small and large spectrum width values and very low SNRs, the variance of the estimated power becomes abnormally large. Nevertheless, simulated time series data with a Gaussian-shaped spectrum are used to investigate the performance of (7) for some special cases. The time series data used were generated following *Torres and Zrnić* [2003], and the performance of the ML technique is examined for variation in SNR, σ_{vn}, and a number of time series samples.

[12] Plots of the bias of the signal power estimate from the ML technique ($\hat{S}_{ML}$) with 100 and 400 time series samples are presented in Figure 1 for variation in normalized spectrum width values ($\sigma_{vn} = \sigma/2v_a$) with v_a as the aliasing velocity. Curves in each plot are generated using 500 realizations and for SNR from −10 to 15 dB at 5 dB intervals. Below the σ_{vn} of 0.2, a positive bias was observed that decreases with an increasing SNR and number of time samples. The bias becomes negative and its magnitude increases with increasing SNR and number of time samples when σ_{vn} is above 0.3. However, the bias is positive when the SNR is −10 dB and the number of time samples is 100. The transition region between being positive and negative bias exists between σ_{vn} 0.2 and 0.3.

[13] Plots of the standard deviation corresponding to retrieved signal power estimate are presented in Figure 2. In general, the standard deviation decreases with increasing number of samples and SNR values. In addition, an asymptotic increase in the standard deviation of the retrieved power is observed below the σ_{vn} of 0.02. A local

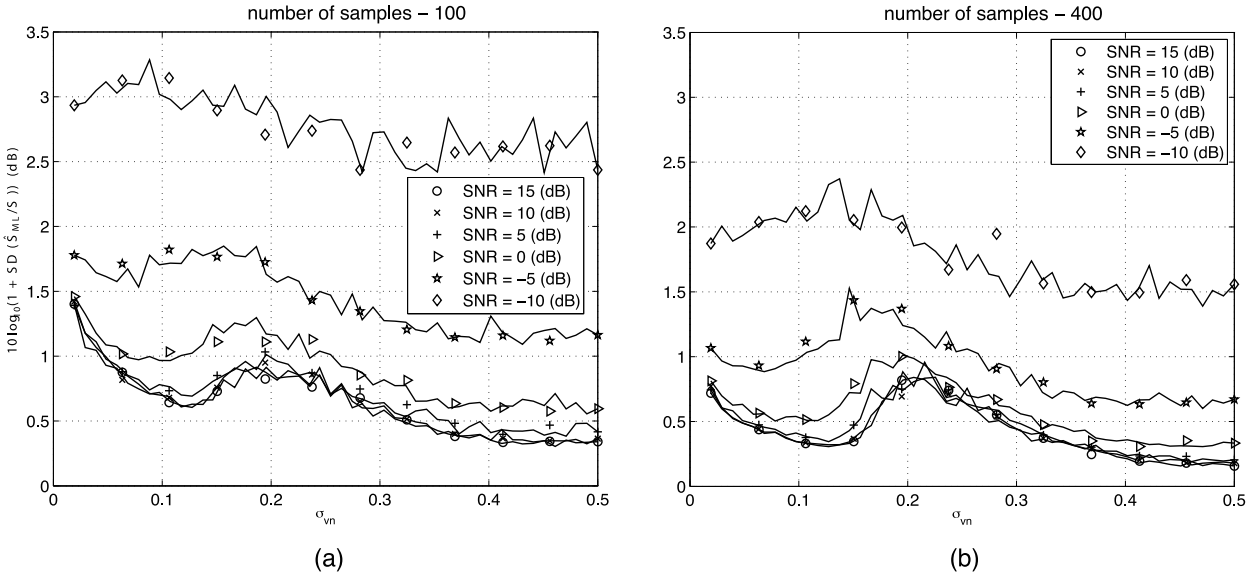

Figure 2. Standard deviation of power estimate obtained using S_{ML} for variation in normalized spectrum width values ($\sigma_{vn} = \sigma/2v_a$). (a) Number of samples − 100. (b) Number of samples − 400. The marked and solid curves are of the same simulated results but are shown for two different resolutions. Investigation of the error statistics revealed that the distribution of the error varies with σ_{vn} and plays a role in shaping the observed bias and standard deviation curves.

maximum is then observed between the σ_{vn} of 0.1 and 0.25, and the magnitude and location of this maximum depend on these parameters. An increase in the SNR or number of samples always shifts this maximum to a larger σ_{vn} and decreases its magnitude, however the shift is asymptotic smaller with increasing SNR and number of samples. The location of the maximum appears to be related to the transition region of the bias. The standard deviation then appears to flatten out when σ_{vn} is larger than 0.3.

[14] Based on statistical analysis in the Appendix B, the effects of the bias and standard deviation of the retrieved power can be shown to be influenced either by the sample size, SNR, σ_{vn}, or the magnitude and ratio of the two lags used in the ML technique. In the case of large normalized spectrum width values, the effects are influenced mainly by $R(2Ts)$ and the lag 2 value that was used. Both factors combined to influence the large bias that was observed. In particular, they manifest as the exponential-shape bias. On the other hand, effects observed at the low normalized spectrum width values are caused by the spectrum width value itself. Because of the term $\frac{1}{\pi^{1/2}\sigma_{vn}^2}$, an asymptotically large increase in the standard deviation is observed at the low spectrum width values. In this analysis, the effect manifests as an asymptotic increase in the standard deviation of the retrieved power. In between the two extreme range of spectrum width values, a combination of both SNR and σ_{vn} influences the results. The degree to which each factor affects the retrieved results depend on the range of σ_{vn} and the SNR level.

3. Application With the Turbulent Eddy Profiler

[15] The Turbulent Eddy Profiler (TEP) is a 915 MHz vertically pointing boundary layer imaging radar developed by the University of Massachusetts [*Mead et al.*, 1998]. The system consists of a 25° beam width transmitting horn antenna and up to 64 receiving subarrays with 32° beam width microstrip patch antennas. This radar was designed to provide fine-scale measurements of the atmospheric boundary layer (ABL) phenomena [*Mead et al.*, 1998]. It has been used to observe turbulent features within the boundary layer in the vertical transport and mixing (VTMX) [*Doran et al.*, 2002] and for comparing results between large eddy simulations and real observations [*Pollard et al.*, 2000]. Additionally, it has been used to investigate airborne clutter sources [*Cheong et al.*, 2006] and precipitation in the boundary layer [*Palmer et al.*, 2005]. Since boundary layer scattering are mainly turbulent in nature when precipitation is not present, the spectral shape of the time series signal is mainly Gaussian and is ideal for applying the ML technique.

[16] The subarrays, shown in Figure 3, were placed in a hexagonal geometry for the processed data. This configuration has an aperture of approximately 4.5 × 4.0 m^2,

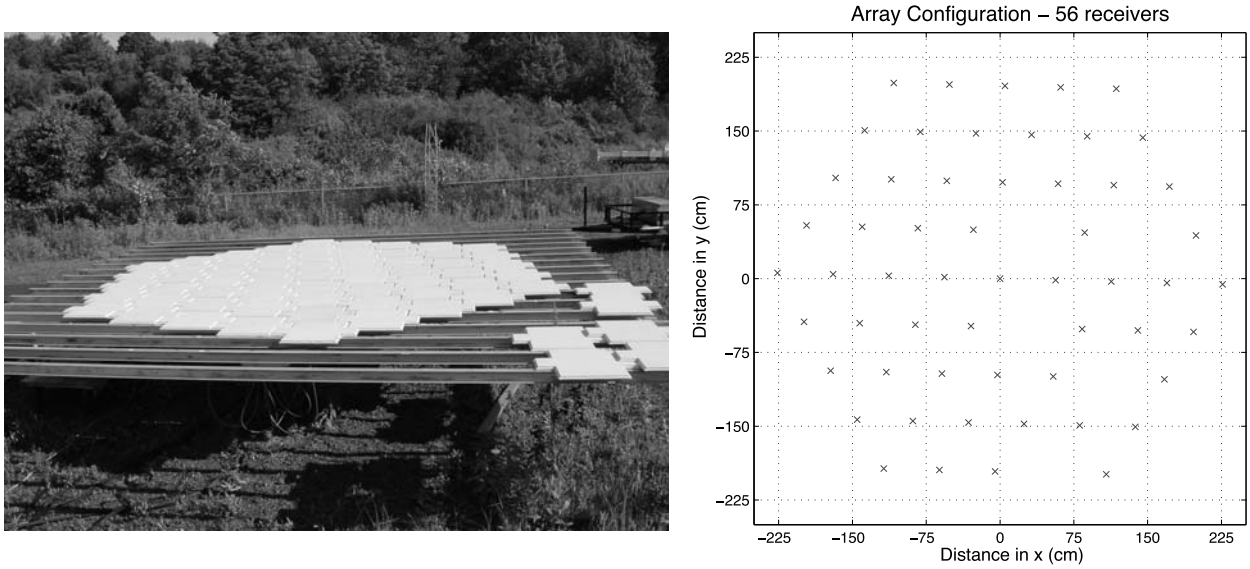

Figure 3. The TEP receiver. (left) A picture of the TEP receiver and the configuration used in the field experiment that collected the processed data set. (right) A plot of the positions of the subarray used. The elements are composed of approximately 64 patch antennas, and the aperture of the receiver in this configuration is approximately 4.5×4.0 m^2.

producing a received beam width of approximately 3.5°. In-depth details of the field experiment were reported by *Cheong et al.* [2006].

[17] A time-height profile of the measured power for 520 time series samples obtained using the ML technique with Capon derived weights is presented in Figure 4 for data recorded between 1435 and 1457 UTC 15 June 2003. Specific details of the coherent averaging approaches were previously discussed by *Palmer et al.* [2005] and *Cheong et al.* [2006]. The measured powers are also presented using pulse-pair-beamforming (PPB) with Fourier (denoted Fourier PPB) and Capon (denoted Capon PPB) weights for comparison. In this profile, the observed atmospheric scatterers are the columnar updrafts associated with superadiabitic heating at the surface and the diffuse downdrafts associated with entrainment at the boundary layer. The observed clutter sources are aerial targets such as birds and insects, the ground, and intermittent sources. Using the adaptive weights, many of the clutter sources are mitigated, as shown in the results from the Capon PPB and ML techniques. In contrast, an aerial target located in the steered position at approximately 1450 UTC and 500 m remains. Additionally, a well-known effect of noise gain caused by inverting the correlation matrix [*Stoica and Moses*, 2005] is evident as a background noise in the result obtained using Capon PPB. This effect has been significantly reduced based on the lower background power level using the ML technique, which is the goal of the proposed multilag technique. At this point, it is noted that the application of Capon PPB may actually result in odd-shaped beams and time series with non-Gaussian statistics, which is problematic for the ML technique. However, since the original Fourier beamforming is assumed to produce time series signals with Gaussian statistics, massaging of the adaptive algorithm such as using diagonal loading to enforce Fourier-like behaviors may be needed. Additionally, the results are again plotted in Figure 5 with the average noise power subtracted. While there are a lot of similarities in the results obtained between the ML and Capon PPB techniques, there are also some noticeable differences that are most observable (located within the dashed lines) at the lower SNR values.

[18] Selected height profiles with times marked in Figure 4 by vertical dashed lines are plotted in Figure 6. They show the evolution of plumes in the boundary layer and provide a quantitative measure of the different retrieved powers using the three techniques. In particular, the evolution of the plumes located between 700–1100 m and between 1450–1700 m are interesting. These echoes are caused by entrained air as equilibrium is restored between thermals and the environmental air and the consequent change in the refractive index gradient. The difference of the retrieved power in these regions using Fourier and Capon PPB is approximately less than 1 dB while it is approximately less than 3 dB using Capon PPB and ML. In addition, the retrieved powers in layers near these two regions using the ML technique are more

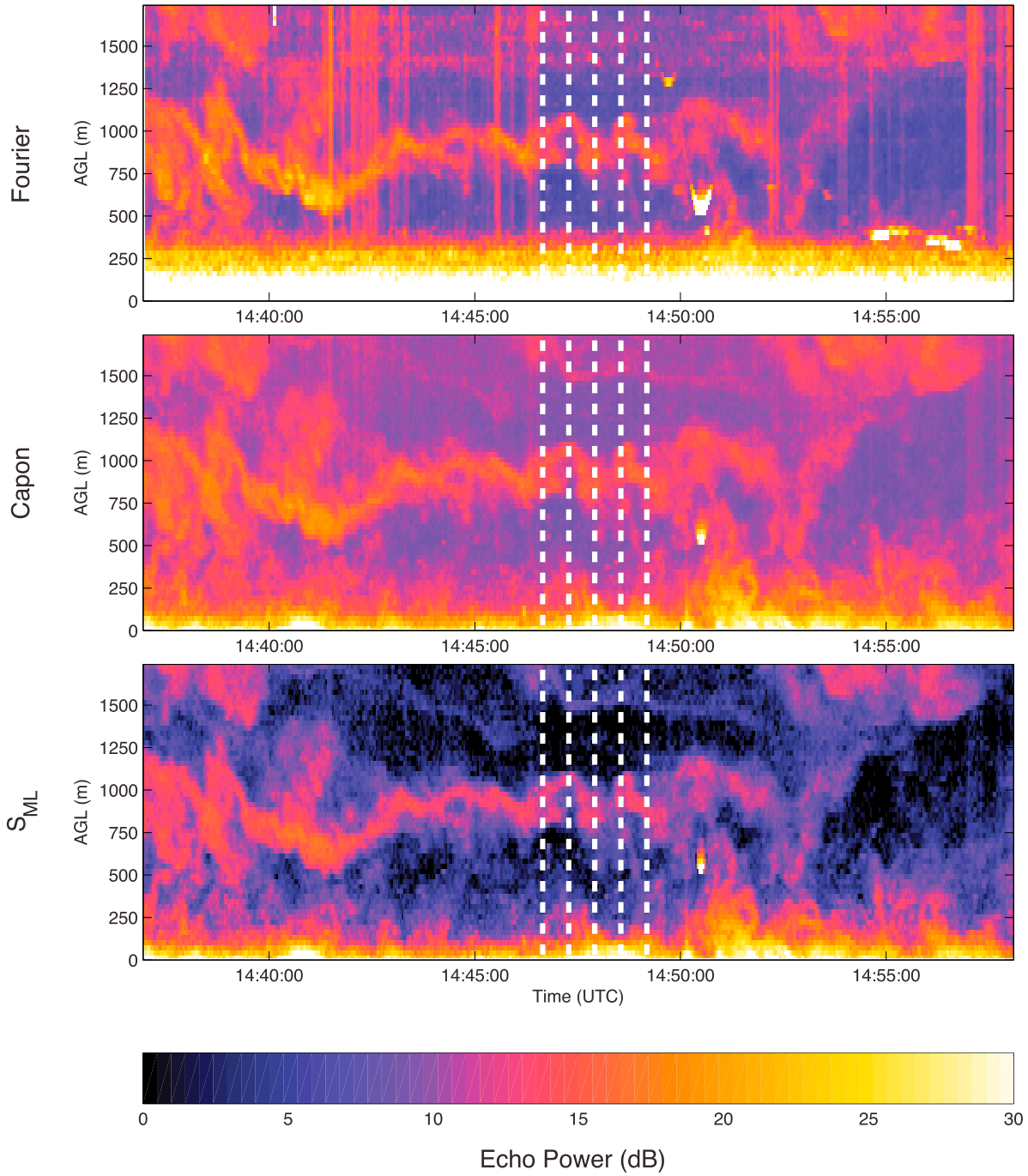

Figure 4. Time-height profile of the measured power for data recorded between 1435 and 1457 UTC 15 June 2003. The profiles are plotted for the measured power obtained using Fourier PPB, Capon PPB, and the ML technique with 520 time samples. Observed atmospheric scatterers include columnar updrafts associated with superadiabitic heating and diffuse downdrafts associated with entrainment.

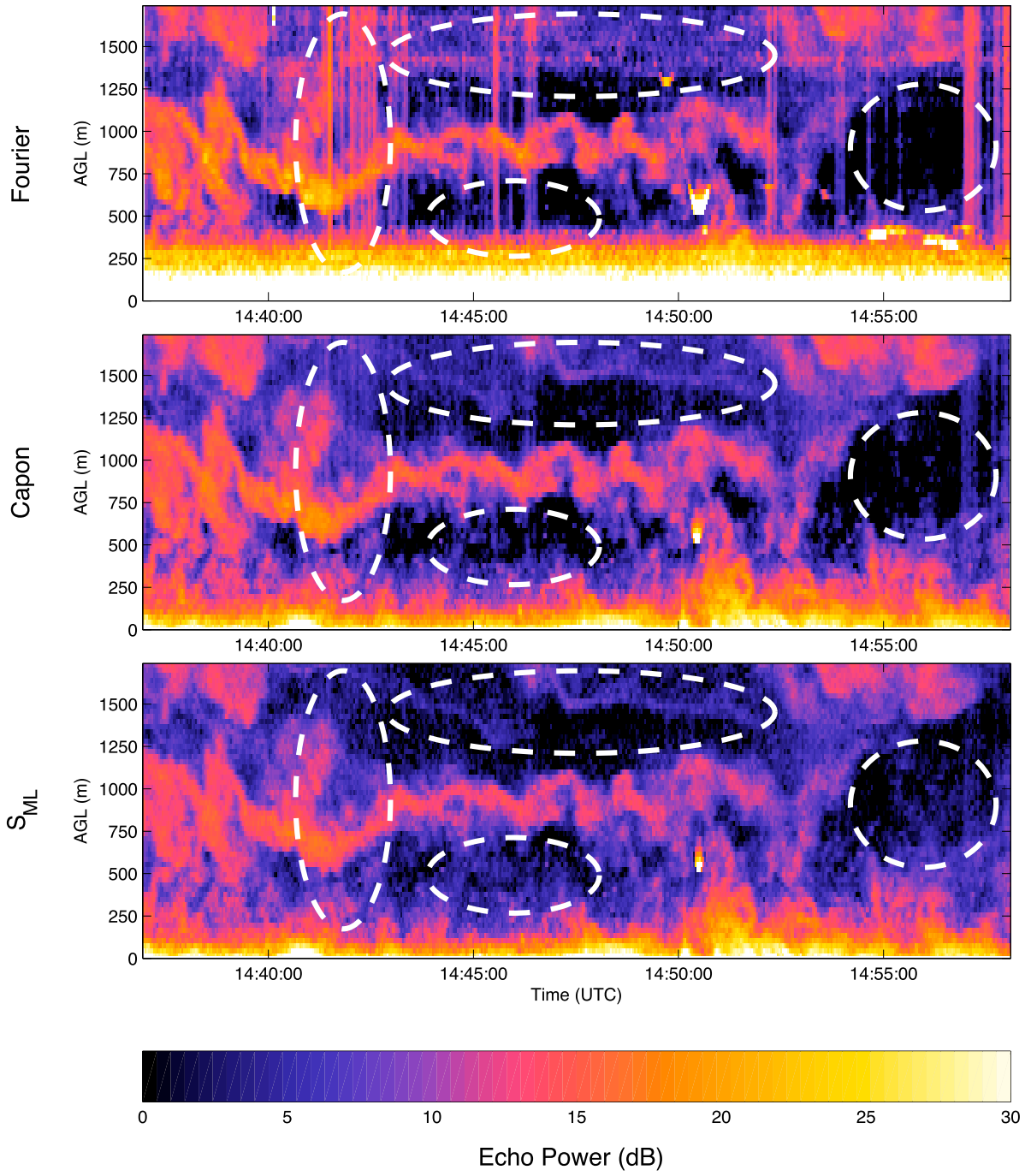

Figure 5. Same as Figure 4, except the average noise power is subtracted from Fourier PBB and Capon PBB. Enclosed in the dashed ovals are some interesting regions with noticeable differences. In these regions, the ML technique appears to produce the most desirable results even though the results themselves are highly variable.

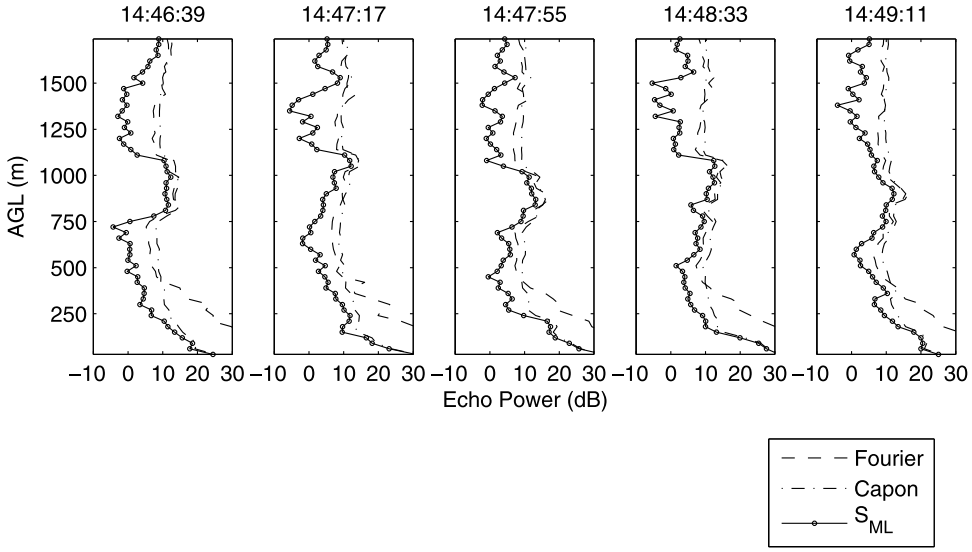

Figure 6. Selected height profiles of the measured power. The retrieved power of times marked in Figure 4 by the vertical dashed lines using Fourier PPB, Capon PPB, and the ML technique are plotted. These profiles show the evolution of plumes in the boundary layer and capture quantitative differences of the retrieved power by the three techniques. A difference of approximately less than 1 dB is observed using Fourier and Capon PPB in the two regions between 700–1100 m and 1450–1700 m. A higher difference of less than 3 dB is obtained using Capon PPB and the ML technique.

sensitive by up to 15 dB as compared to the results obtained using Capon and Fourier PPB based on the weakest retrieved power level. Weak atmospheric scatterers are masked by the noise level and are difficult to identify in the results obtained using Capon and Fourier PPB.

[19] Along with the vertical slices, cross-section images showing the two-dimensional structure of the plumes along the zonal direction are presented in Figure 7 for the selected times. While the structures of the plume located between 700 and 1100 m are resolved using all three techniques, the spatially discontinuous power features in the region between 1450 and 1700 m interfere with the results obtained using Fourier PPB. These features are signatures of clutter contamination and make it difficult to identify the atmospheric scatterers in this region. The atmospheric scatterers in this region are easier to resolve in the results obtained using Capon PPB and the ML technique with adaptive weights. In addition, the adaptive weights enhanced the near ground atmospheric scattered signal below 400 m. Scattering from the boundary layer heating that connects to the plumes located between 700 and 1100 m were observed in the results obtained using the Capon PPB and the ML technique, whereas they were masked by the ground clutter in the results obtained using Fourier PPB.

[20] Scatterplot comparisons of the measured powers obtained in Figure 4 are presented in Figure 8 to investigate the sensitivity of the three techniques. A plot was generated for the results obtained using Capon PPB and the ML technique and another for Fourier PPB and the ML technique. In the results obtained using Capon PPB and the ML technique, an approximately linear relationship with a decreasing positive bias toward Capon PPB and a decreasing spread was observed when the Capon PPB increases above 10 dB. Below this threshold, the values obtained using Capon PPB are approximately constant while the values obtained using the ML technique can be as low as −10 dB. The results observed above this threshold are similar to the changes mentioned of the bias and variance in section 2.2 when σ_{vn} is between 0.1 and 0.3 and the parameter SNR was varied. In the simulations, it was observed that the bias and variance decreased with increasing SNR. In this case, the SNR is approximately related to the Capon PPB power values. The results obtained when the Capon PPB retrieved powers are below 10 dB highlight the enhanced sensitivity obtained using the ML technique. While the Capon PPB technique is limited to scatterers with measured power of at least 10 dB, the ML technique is sensitive to weaker scatterers. On the other hand, the results of the scatterplot for the Fourier PPB and ML technique show the effects of using adaptive weights and its clutter rejection capability in addition to the enhanced sensitivity effects. The scattered power of the Fourier PPB results above 15 dB generally consist of ground clutter and its value is biased away toward Fourier PPB from the expected linear line. Moreover, the results

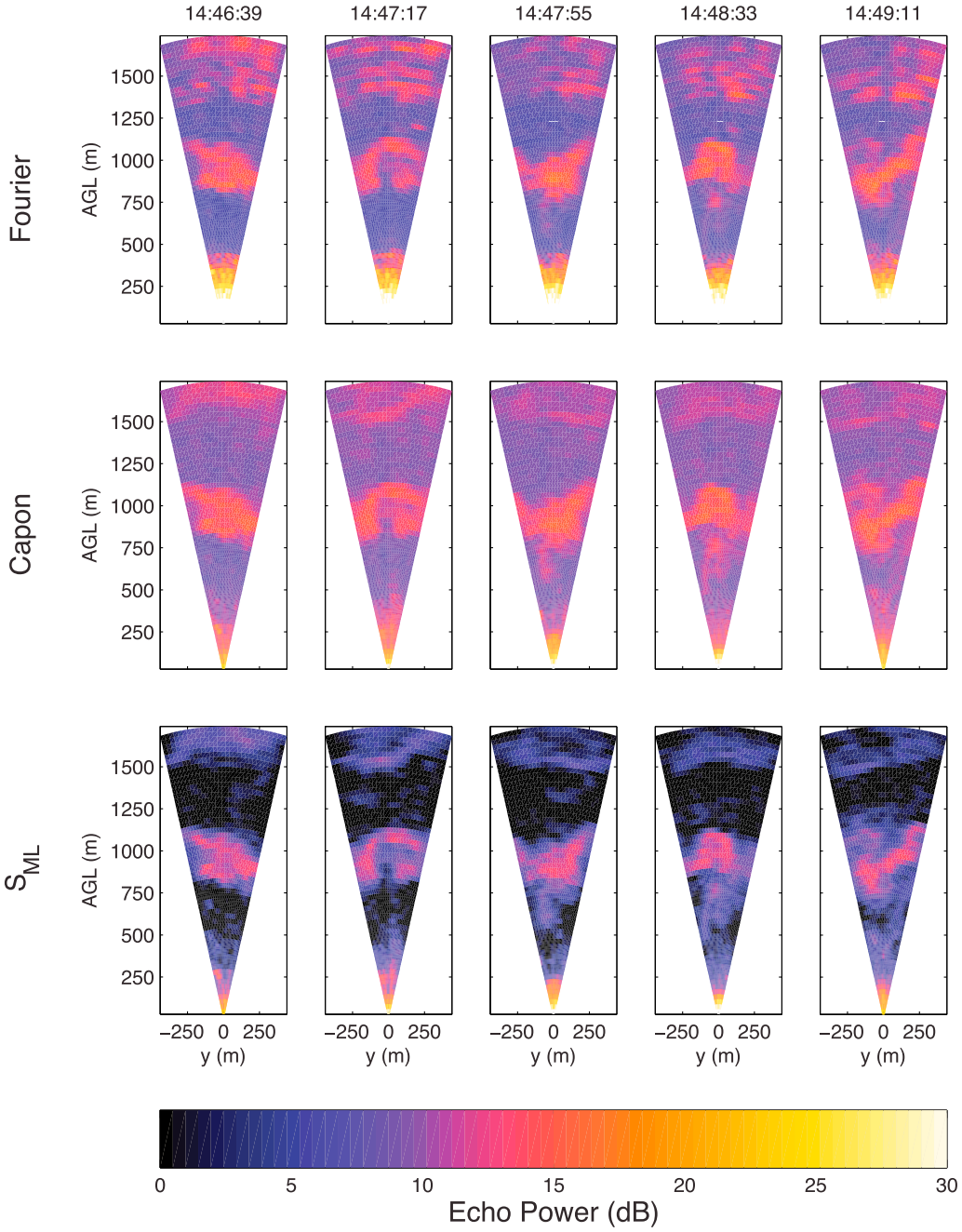

Figure 7. Selected cross sections of the measured power. The retrieved power of times marked in Figure 4 by the vertical dashed lines are plotted using Fourier PPB, Capon PPB, and the ML technique. These images show the two-dimensional structure of the plumes along the zonal direction and benefits of using adaptive weights. The atmospheric scattering between 1450 and 1700 m and near the ground were observed using the Capon PPB and the ML technique, whereas they were masked in the results obtained using Fourier PPB.

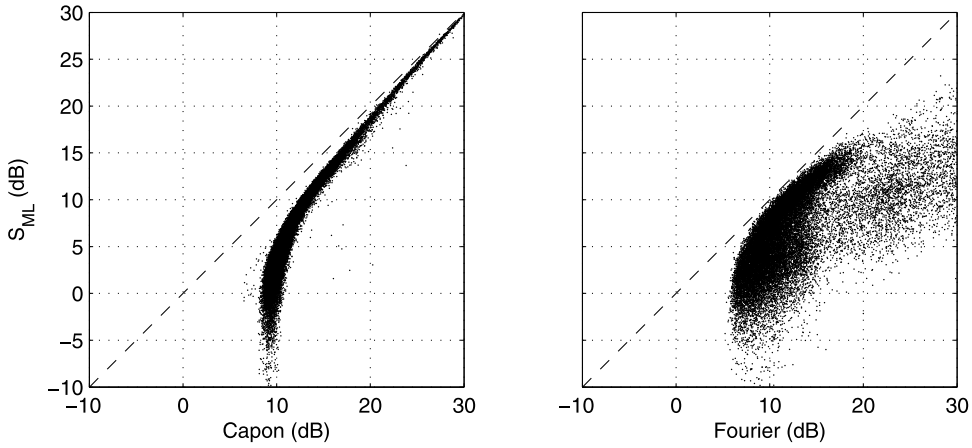

Figure 8. Scatterplots of measured power obtained in Figure 4. A plot was generated for the results obtained using Capon PPB and the ML technique, and another was generated for Fourier PPB and the ML technique. The results obtained using Capon PPB and the ML technique show an approximately linear relationship with a decreasing positive bias toward Capon PPB, and a decreasing spread was observed when the Capon PPB increases above 10 dB. Below this threshold, the values obtained using Capon PPB are approximately constant while the values obtained using the ML technique can be as low as −10 dB. These results highlight the enhanced sensitivity obtained using the ML technique. The results of the Fourier PPB and ML scatterplot show the effects of using adaptive weights and its clutter rejection capability in addition to the enhanced sensitivity effects.

obtained is always lower using the ML technique than Fourier PPB and show the adaptive nature of the weights and its desire to reduce the overall power even in the region with atmospheric scatterers between 10 and 20 dB.

4. Conclusions

[21] An ML technique was introduced for retrieving the measuring power without the need to estimate the noise power. The technique was derived using an array model, and a special case using lags 1 and 2 was presented. The performance of the ML technique using lags 1 and 2 in terms of bias and standard deviation was investigated using numerical simulation generated following *Torres and Zrnić* [2003]. Results of the bias and standard deviation were plotted with 100 and 400 time series samples, normalized spectrum width values from 0.01 to 0.5, and an SNR ranging from −10 to 15 dB. Additionally, a general two-lag technique was presented and its statistics was examined using perturbation analysis. Based on these results, the effects of the bias and standard deviation of the retrieved power was shown to be affected by the sample size, SNR, σ_{vn}, or the magnitude and ratio of the two lags used in the ML technique. In the case of large normalized spectrum width values, the effects are influenced mainly by the variance of the larger correlation value and the lag ratio that were used. On the other hand, effects at the low normalized spectrum width values are caused by the spectrum width value itself. In between the two extreme range of spectrum width values, a combination of both SNR and σ_{vn} influences the results. Additionally, the ML technique was then applied to real data collected between 1435 and 1457 UTC 15 June 2003 using the Turbulent Eddy Profiler of atmospheric boundary layer scattering. The results were plotted using time-height profiles, cross-sections images, and scatterplots, and the results were compared to the retrieved power obtained using Fourier and Capon PPB. The results showed the benefits of the adaptive weights and the enhanced sensitivity in terms of the minimum power detected of the retrieval technique. The ML technique was able to mitigate the intermittent clutter sources and resolve atmospheric scatterers in the region between 1450 and 1700 m, and attenuate some of the ground clutter to resolve the weak near ground scattering below 400 m based on the decreased power that was observed. Moreover, an enhancement of up to 15 dB was observed in the transition regions around 700–1100 m and 1450–1700 m. Using this relatively simple idea of multilag correlation, the proposed technique has been shown to enhance the retrieval of weak atmospheric signals with Gaussian spectra. Future work will include investigation of the ML technique for retrieving the reflectivity value observed using weather radars. In addition, studies of the performance of the ML technique are needed under conditions with signals that may not have Gaussian spectra.

Appendix A: Assumed Correlation Matrix Structure

[22] Assume that the temporal correlation of the ith signal source is given by

$$R_i(mT_s) = E\{s^*(nT_s)s((m+n)T_s)\} = S_i \exp\left[-8(\pi\sigma_{v_i} mT_s/\lambda)^2\right] \exp\left[-j4\pi v_i mT_s/\lambda\right], \tag{A1}$$

where S_i is the power, σ_{vi} is the spectrum width, v_i is the Doppler velocity, and λ is the wavelength. Furthermore, assume that the sources are uncorrelated for $m \neq 0$. The data covariance matrix of the array signals is then

$$\mathbf{R}_x(mT_s) = \mathbf{A}\mathbf{R}_s(mT_s)\mathbf{A}^H + N\mathbf{I}\delta_m, \tag{A2}$$

where

$$\mathbf{R}_s(mT_s) = \begin{bmatrix} R_1(mT_s) & 0 & \cdots & 0 \\ 0 & R_2(mT_s) & 0 & \vdots \\ \vdots & \ddots & \ddots & \ddots \\ 0 & \cdots & 0 & R_d(mT_s) \end{bmatrix}, \tag{A3}$$

N is the noise power, and δ_m is the Kronecker delta function. Then, it can be shown that

$$\mathbf{R}_s(mT_s) = \mathbf{R}_s(0) \otimes \mathbf{C}(mT_s). \tag{A4}$$

Likewise,

$$\mathbf{R}_s(0) = \mathbf{R}_s(mT_s) \otimes \mathbf{C}^{-1}(mT_s), \tag{A5}$$

where

$$\mathbf{C}(mT_s) = \begin{bmatrix} C_{11} & 0 & \cdots & 0 \\ 0 & C_{21} & 0 & \vdots \\ \vdots & \ddots & \ddots & \ddots \\ 0 & \cdots & 0 & C_{d1} \end{bmatrix} \otimes \begin{bmatrix} C_{12} & 0 & \cdots & 0 \\ 0 & C_{22} & 0 & \vdots \\ \vdots & \ddots & \ddots & \ddots \\ 0 & \cdots & 0 & C_{d2} \end{bmatrix}, \tag{A6}$$

where $\otimes$ denotes the Kronecker product, $C_{i1} = \exp -8[\pi\sigma_{vi} mT_s/\lambda]^2$, and $C_{i2} = \exp[-j4\pi v_i mT_s/\lambda]$.

Appendix B: Variance of ML Estimator Using Ratio of Two Lags

[23] The power S can be described using a ratio of two lags from $R(m'') = R_s(m'') + R_n(m'')$, where $R_s(m'') = S\exp[-2(\pi\sigma_{vn}m'')^2 + j2\pi v_n m'']$ and $R_n(m'') = N\delta_{m''},0$, through the equation

$$S = \left(\frac{|R(m')|^A}{|R(m'')|}\right)^B = \left(\frac{S^A \exp\left[-m'^2 A\right]}{S\exp\left[-m''^2\right]}\right)^B, \tag{B1}$$

where $m' > m'' \geq 1$, $-m'^2 A + m''^2 = 0$. Note that $v_n = v/2v_a$ is used while T_s is already incorporated using v_a. This gives $A = \frac{m''^2}{m'^2}$, $A > 0$, and $B = \frac{1}{A-1}$, $1 > B > 0$. Its variance is

$$\mathrm{var}\{\hat{S}\} = (C_1)^2 \mathrm{var}\{|\hat{R}(m')|\} + (C_2)^2 \mathrm{var}\{|\hat{R}(m'')|\} + 2C_1C_2 \mathrm{cov}\{|\hat{R}(m')|, |\hat{R}(m'')|\}, \tag{B2}$$

where

$$C_1 \equiv \frac{\partial S}{\partial |R(m')|} = AB|R(m')|^{AB-1}|R(m'')|^{-B} \tag{B3}$$

and

$$C_2 = \frac{\partial S}{\partial |R(m'')|} = -B|R(m')|^{AB}|R(m'')|^{-B-1} \tag{B4}$$

Values of the above three terms can be obtained through perturbation analysis and by assuming that the correlation function has an expected value and a zero mean perturbation. With this, the covariance of the absolute value of the correlation for any two lags is

$$\mathrm{cov}\{|\hat{R}(m')|, |\hat{R}(m'')|\} \approx |R(m')||R(m'')| \cdot \frac{1}{4} E\left\{\frac{\triangle R(m')\triangle R(m'')}{R(m')R(m'')} + \frac{\triangle R^*(m')\triangle R(m'')}{R^*(m')R(m'')} + \frac{\triangle R(m')\triangle R^*(m'')}{R(m')R^*(m'')} + \frac{\triangle R^*(m')\triangle R^*(m'')}{R^*(m')R^*(m'')}\right\} \tag{B5}$$

To solve the above problem, use a solution found in the work of *Zhang et al.* [2004] of

$$\sum_{M-1}^{M-1}(M-|n''|)R(n'')R(-n''+m'-m'') \approx \frac{MS^2}{2\pi^{1/2}\sigma_{vn}}\exp\left[-\pi^2\sigma_{vn}^2(m'-m'')^2\right] \cdot \exp[j2\pi v_n(m'-m'')] + 2R_s(m'-m'')MN + MN^2\delta_{m'-m'',0} \quad \text{(B6)}$$

Solving for a general case of

$$\begin{aligned}
E\{\triangle R(m')\triangle R^*(m'')\} &= E\left\{\left(\frac{1}{M}\sum_{n=0}^{M-1}X^*(n)X(n+m')-R(m')\right)\cdot\left(\frac{1}{M}\sum_{n'=0}^{M-1}X^*(n')X(n'+m'')-R(m'')\right)^*\right\}\\
&= E\left\{\frac{1}{M}\sum_{n=0}^{M-1}\sum_{n'=0}^{M-1}X^*(n)X(n+m')X(n')X^*(n'+m'')\right\}\\
&\quad - E\left\{\frac{1}{M}\sum_{n=0}^{M-1}X^*(n)X(n+m')R^*(m'')\right\}\\
&\quad - E\left\{\frac{1}{M}\sum_{n'=0}^{M-1}X(n')X^*(n'+m'')R(m')\right\}\\
&\quad + R(m')R^*(m'')\\
&= E\left\{\frac{1}{M^2}\sum_{n=0}^{M-1}\sum_{n'=0}^{M-1}X^*(n)X(n+m')X(n')X^*(n'+m'')\right\}\\
&\quad - R(m')R^*(m'') - R(-m'')R(m') + R(m')R^*(m'')\\
&= \frac{1}{M^2}\sum_{n=0}^{M-1}\sum_{n'=0}^{M-1}E\{X^*(n)X(n')\}E\{X(n+m')X^*(n'+m'')\}\\
&\quad - R(m')R^*(m'') - R(-m'')R(m') + 2R(m')R^*(m'')\\
&= \frac{1}{M^2}\sum_{n=0}^{M-1}\sum_{n'=0}^{M-1}R(n'-n)R(n+m'-n'-m'')\\
&= \frac{1}{M^2}\sum_{n''=-M+1}^{M-1}(M-|n''|)R(n'')R(-n''+m'-m'')\\
&= \frac{1}{M^2}\left[\frac{MS^2}{2\pi^{1/2}\sigma_{vn}}\exp\left[-\pi^2\sigma_{vn}^2(m'-m'')^2\right]\exp[j2\pi v_n(m'-m'')]\right.\\
&\quad \left. + 2R_s(m'-m'')MN + MN^2\delta_{m'-m'',0}\right]. \quad \text{(B7)}
\end{aligned}$$

The above solution is then used to calculate the components of the covariance, i.e.,

$$\begin{aligned}
E\{\triangle R(m')\triangle R(m'')\} &= E\{\triangle R(m')\triangle R^*(-m'')\}\\
&= \frac{1}{M^2}\left[\frac{MS^2}{2\pi^{1/2}\sigma_{vn}}\exp\left[-\pi^2\sigma_{vn}^2(m'+m'')^2\right]\right.\\
&\quad \left.\cdot\exp[j2\pi v_n(m'+m'')]+2R_s(m'+m'')MN + MN^2\delta_{m'+m'',0}\right] \quad \text{(B8)}
\end{aligned}$$

and

$$E\{\triangle R(m')\triangle R^*(m'')\} = E\{\triangle R(m')\triangle R^*(m'')\}$$
$$= \frac{1}{M^2}\left[\frac{MS^2}{2\pi^{1/2}\sigma_{vn}}\exp\left[-\pi^2\sigma_{vn}^2(m'-m'')^2\right]\right.$$
$$\left.\cdot\exp[j2\pi v_n(m'-m'')] + 2R_s(m'-m'')MN + MN^2\delta_{m'-m'',0}\right] \quad \text{(B9)}$$

and

$$E\{\triangle R^*(m')\triangle R^*(m'')\}$$
$$= E\{\triangle R(-m')\triangle R^*(m'')\}$$
$$= \frac{1}{M^2}\left[\frac{MS^2}{2\pi^{1/2}\sigma_{vn}}\exp\left[-\pi^2\sigma_{vn}^2(-m'-m'')^2\right]\right.$$
$$\cdot\exp[j2\pi v_n(-m'-m'')]$$
$$\left.+\ 2R_s(-m'-m'')MN + MN^2\delta_{-m'-m'',0}\right]. \quad \text{(B10)}$$

Therefore,

$$\frac{|R(m')||R(m'')|}{R(m')R(m'')}E\{\triangle R(m')\triangle R(m'')\}$$
$$= \exp[-j2\pi v_n(m'+m'')]\cdot E\{\triangle R(m')\triangle R(m'')\}$$
$$= \frac{1}{M^2}\left[\frac{MS^2}{2\pi^{1/2}\sigma_{vn}}\right.$$
$$\cdot\exp\left[-\pi^2\sigma_{vn}^2(m'+m'')^2\right]$$
$$\cdot\ \exp[j2\pi v_n(m'+m'')] + 2R_s(m'+m'')MN$$
$$\left.+\ MN^2\delta_{m'+m'',0}\right]$$
$$= \frac{1}{M^2}\left[\frac{MS^2}{2\pi^{1/2}\sigma_{vn}}\exp\left[-\pi^2\sigma_{vn}^2(m'+m'')^2\right]\right.$$
$$+\ 2|R_s(m'+m'')|MN$$
$$\left.+\ MN^2\delta_{m'+m'',0}\right] \quad \text{(B11)}$$

and

$$\frac{|R(m')||R(m'')|}{R(m')R^*(m'')}E\{\triangle R(m')\triangle R^*(m'')\}$$
$$= \exp[-j2\pi v_n(m'-m'')]\cdot E\{\triangle R(m')\triangle R^*(m'')\}$$
$$= \frac{1}{M^2}\left[\frac{MS^2}{2\pi^{1/2}\sigma_{vn}}\exp\left[-\pi^2\sigma_{vn}^2(m'-m'')^2\right]\right.$$
$$\left.+\ 2|R_s(m'-m'')|MN + MN^2\delta_{m'-m'',0}\right] \quad \text{(B12)}$$

and

$$\frac{|R(m')||R(m'')|}{R^*(m')R^*(m'')}E\{\triangle R^*(m')\triangle R^*(m'')\}$$
$$= \exp[-j2\pi v_n(-m'-m'')]\cdot E\{\triangle R(-m')\triangle R^*(m'')\}$$
$$= \frac{1}{M^2}\left[\frac{MS^2}{2\pi^{1/2}\sigma_{vn}}\exp\left[-\pi^2\sigma_{vn}^2(-m'-m'')^2\right]\right.$$
$$+\ 2|R_s(-m'-m'')|MN$$
$$\left.+\ MN^2\delta_{-m'-m'',0}\right]. \quad \text{(B13)}$$

By applying the above three equations, the covariance of the absolute correlation value between any two arbitrary lags is

$$\mathrm{cov}\{|\hat{R}(m')|,|\hat{R}(m'')|\} = \frac{1}{4M^2}\left[\frac{MS^2}{\pi^{1/2}\sigma_{vn}}\right.$$
$$\cdot\exp\left[-\pi^2\sigma_{vn}^2(m'+m'')^2\right]$$
$$+\frac{MS^2}{\pi^{1/2}\sigma_{vn}}\exp\left[-\pi^2\sigma_{vn}^2(m'-m'')^2\right]$$
$$+4|R_s(m'+m'')|MN + 4|R_s(m'-m'')|MN$$
$$\left.+\ 2MN^2\delta_{m'+m'',0} + 2MN^2\delta_{m'-m'',0}\right]. \quad \text{(B14)}$$

Let SNR $\equiv \frac{S}{N}$. For $m' \neq m''$, $m' \geq 1$, $m'' \geq 1$,

$$\mathrm{cov}\{|\hat{R}(m')|,|\hat{R}(m'')|\} = \frac{S^2}{4M}\left[\frac{\exp\left[-\pi^2\sigma_{vn}^2(m'+m'')^2\right]}{\pi^{1/2}\sigma_{vn}}\right.$$
$$+\frac{\exp\left[-\pi^2\sigma_{vn}^2(m'-m'')^2\right]}{\pi^{1/2}\sigma_{vn}} + \frac{4\exp\left[-2\pi^2\sigma_{vn}^2(m'+m'')^2\right]}{\mathrm{SNR}}$$
$$+\frac{4\exp\left[-2\pi^2\sigma_{vn}^2(m'-m'')^2\right]}{\mathrm{SNR}} + \frac{2}{\mathrm{SNR}^2}\delta_{m'+m'',0}$$
$$\left.+\ 2\frac{1}{\mathrm{SNR}^2}\delta_{m'-m'',0}\right] \approx \frac{S^2}{4M}\left[\frac{\exp\left[-\pi^2\sigma_{vn}^2(m'-m'')^2\right]}{\pi^{1/2}\sigma_{vn}}\right.$$
$$\left.+\frac{4\exp\left[-2\pi^2\sigma_{vn}^2(m'-m'')^2\right]}{\mathrm{SNR}}\right] \quad \text{(B15)}$$

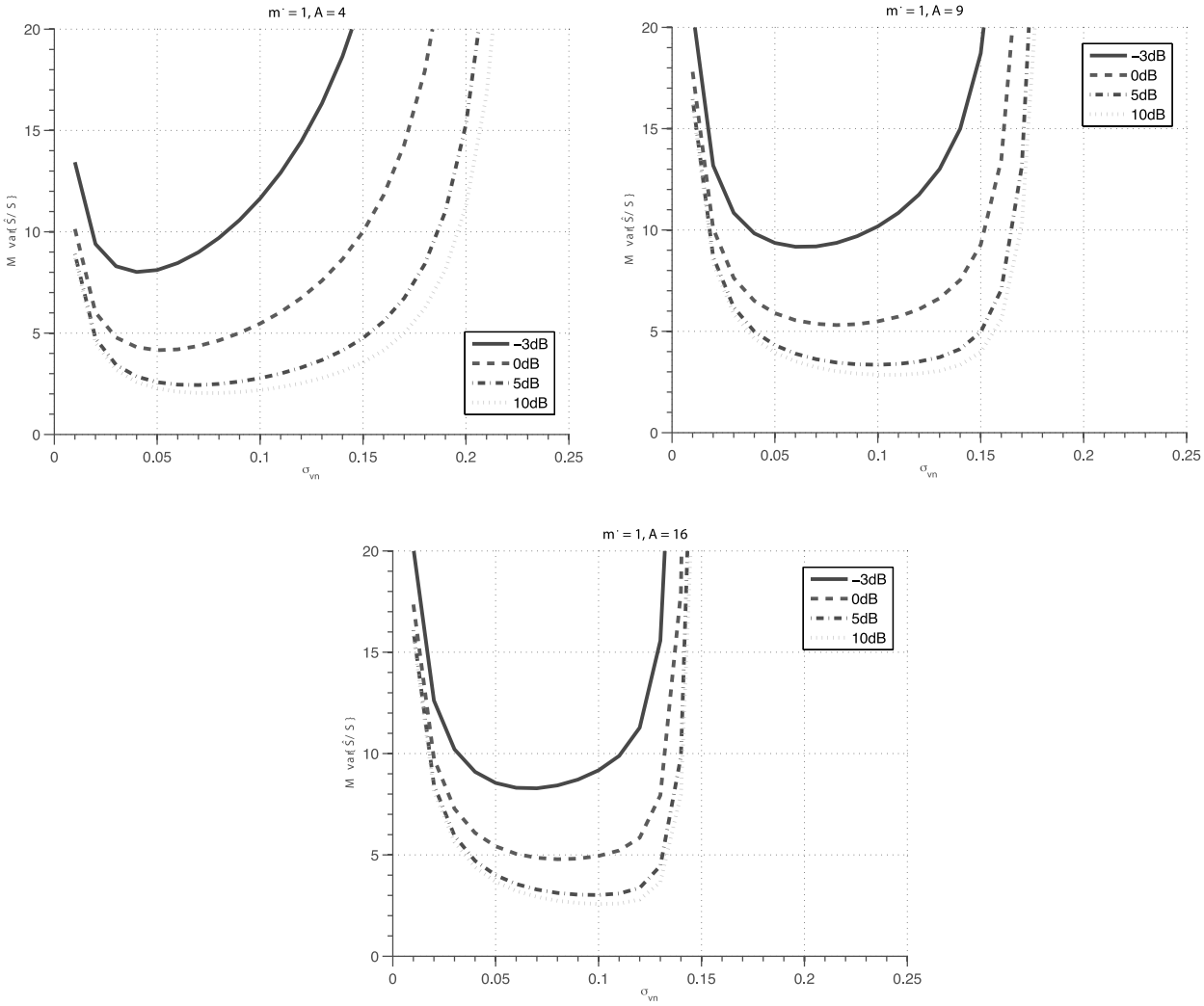

Figure B1. Statistical analysis of retrieved power variance. The results are shown for $m' = 1$ and $m'' = 2$, 3, and 4. The values are asymptotically large at small and large values of normalized spectrum widths and are minimal somewhere in between. This trend limits the retrieval technique to echo signals with moderate values of normalized spectrum widths.

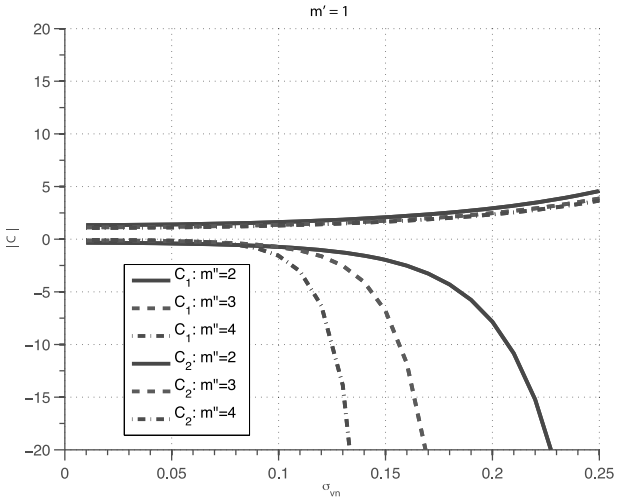

Figure B2. Values of C_1 and C_2 for $m' = 1$ and $m'' = 1, 2$, and 3. When squared and then multiplied with the variance of its perturbation, the result is the autocovariance. In this plot, the asymptotically negative curves are those obtained for with C_2, and the other curves are those of C_1.

and

$$\operatorname{cov}\{|\hat{R}(m')|, |\hat{R}(m')|\} = \frac{S^2}{4M}\left[\frac{\exp\left[-\pi^2\sigma_{vn}^2(2m')^2\right]}{\pi^{1/2}\sigma_{vn}} + \frac{1}{\pi^{1/2}\sigma_{vn}} + \frac{4\exp\left[-2\pi^2\sigma_{vn}^2(2m')^2\right]}{\mathrm{SNR}} + \frac{4}{\mathrm{SNR}} + \frac{2}{\mathrm{SNR}^2}\right]$$
$$\approx \frac{S^2}{4M}\left[\frac{1}{\pi^{1/2}\sigma_{vn}} + \frac{4}{\mathrm{SNR}} + \frac{2}{\mathrm{SNR}^2}\right]. \quad \text{(B16)}$$

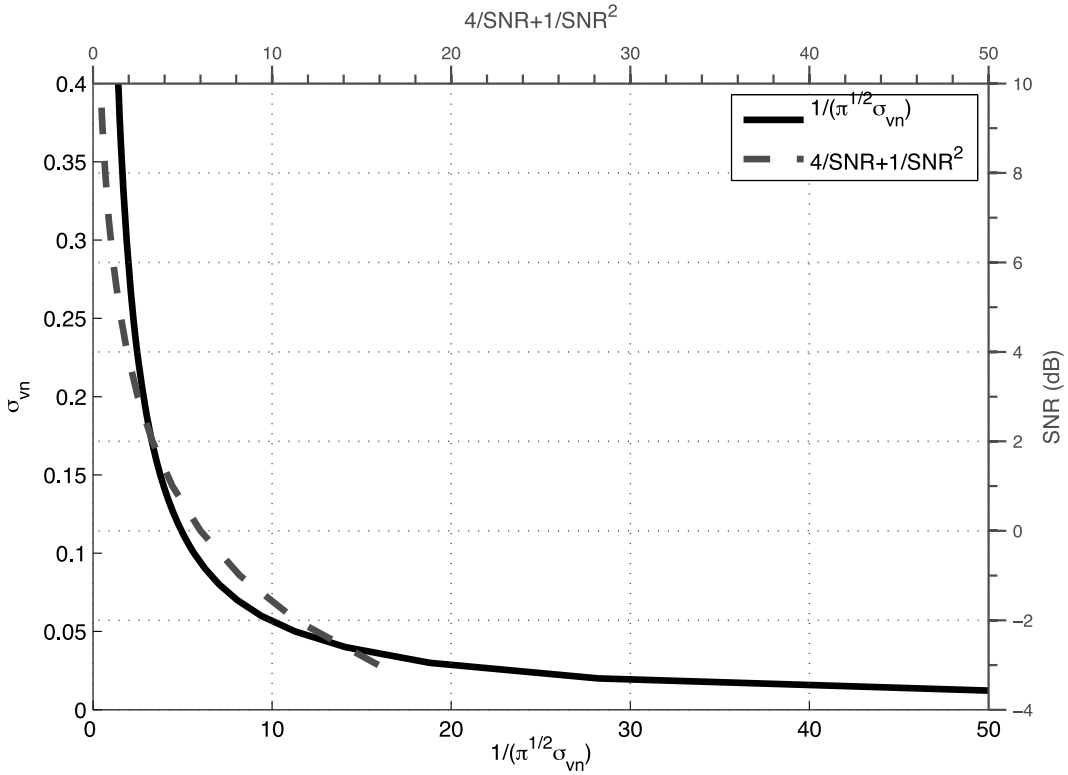

Figure B3. Values of $\frac{1}{\pi^{1/2}\sigma_{vn}}$ and $\frac{4}{\mathrm{SNR}} + \frac{2}{\mathrm{SNR}^2}$ for various ranges of *SNR* and σ_{vn}. These two terms are used to calculate C_1 and C_2. The results show that $\frac{1}{\pi^{1/2}\sigma_{vn}}$ is larger than $\frac{4}{\mathrm{SNR}} + \frac{2}{\mathrm{SNR}^2}$ for all cases except those with moderately low SNRs.

So

$$\begin{aligned}\mathrm{var}\{\hat{S}\} &\approx \left(C_1{}^2 + C_2{}^2\right)\left[\frac{S^2}{4M}\left[\frac{1}{\pi^{1/2}\sigma_{vn}} + \frac{4}{\mathrm{SNR}} + \frac{2}{\mathrm{SNR}^2}\right]\right] \\ &\quad + 2C_1C_2\frac{S^2}{4M}\left[\frac{\exp\left[-\pi^2\sigma_{vn}^2(m'-m'')^2\right]}{\pi^{1/2}\sigma_{vn}}\right. \\ &\quad \left. + \frac{4\exp\left[-2\pi^2\sigma_{vn}^2(m'-m'')^2\right]}{\mathrm{SNR}}\right]. \\ &= \left(C_1{}^2 + C_2{}^2\right)\left[\frac{S^2}{4M}\left[\frac{1}{\pi^{1/2}\sigma_{vn}} + \frac{4}{\mathrm{SNR}} + \frac{2}{\mathrm{SNR}^2}\right]\right] \\ &\quad + 2C_1C_2\frac{S^2}{4M}\left[\frac{\exp\left[-\pi^2\sigma_{vn}^2m'^2(1-A)^2\right]}{\pi^{1/2}\sigma_{vn}}\right. \\ &\quad \left. + \frac{4\exp\left[-2\pi^2\sigma_{vn}^2m'^2(1-A)^2\right]}{\mathrm{SNR}}\right]. \end{aligned} \tag{B17}$$

where

$$\begin{aligned}C_1 &= AB|R(m')|^{AB-1}|R(m'')|^{-B} \\ &= AB|R(m')|^{(AB-1)}|R(m'')|^{-B} \\ &= ABS^{(AB-1)}\exp\left[-2(AB-1)(\pi\sigma_{vn}m')^2\right] \\ &\quad \cdot\ S^{-B}\exp\left[2(B)(\pi\sigma_{vn}m'')^2\right] \\ &= ABS^{(AB-1)-B}\exp\left[-\left(2(AB-1)m'^2 - 2(B)m''^2\right)\right. \\ &\quad \left.\cdot\ (\pi\sigma_{vn})^2\right] \end{aligned} \tag{B18}$$

where

$$\begin{aligned}(AB-1) - B &= \left(A\frac{1}{A-1} - 1\right) - \frac{1}{A-1} \\ &= 0 \end{aligned} \tag{B19}$$

and

$$\begin{aligned}-\left(2(AB-1)m'^2 - 2Bm''^2\right) &= -2m'^2\left((AB-1) - B\frac{m''^2}{m'^2}\right) \\ &= -2m'^2((AB-1) - BA) \\ &= 2m'^2. \end{aligned} \tag{B20}$$

So,

$$(C_1)^2 = \left(\frac{A}{A-1}\right)^2\exp\left[4m'^2(\pi\sigma_{vn})^2\right]. \tag{B21}$$

Similarly,

$$\begin{aligned}C_2 &= -B|R(m')|^{AB}|R(m'')|^{-B-1} \\ &= BS^{(AB)}\exp\left[-2(AB)(\pi\sigma_{vn}m')^2\right]S^{-B-1)} \\ &\quad \cdot\ \exp\left[2(B+1)(\pi\sigma_{vn}m')^2\right] \\ &= BS^{(AB)-B-1}\exp\left[-2\left(ABm'^2 - (B+1)m''^2\right)(\pi\sigma_{vn})^2\right] \end{aligned} \tag{B22}$$

where

$$\begin{aligned}-2\left(ABm'^2 - (B+1)m''^2\right) &= -2m'^2\left(AB - (B+1)\frac{m''^2}{m'^2}\right) \\ &= -2m'^2(AB - (B+1)A) \\ &= 2Am'^2. \end{aligned} \tag{B23}$$

So,

$$(C_2)^2 = \left(\frac{1}{A-1}\right)^2\exp\left[4Am'^2(\pi\sigma_{vn})^2\right]. \tag{B24}$$

[24] Several cases showing the variance of the retrieved power are plotted in Figure B1. Values of $m' = 1$ and $m'' = 2$, 3, and 4 and SNR of -3, 0, 5, and 10 dB were used to obtain the results. The variance is asymptotically large at small and large values of normalized spectrum widths and its minimum is located at spectrum widths with values ranging between 0.02 and 0.2. By observing the magnitude of C_1 and C_2 shown in Figure B2, the upper limit of the variance can be inferred. The asymptotic limit is caused by C_2 and it decreases with increasing m'' at an exponentially squared rate. On the other hand, the lower limit can be inferred by looking at the results in Figure B3. At the low spectrum width, the term $\frac{1}{\pi^{1/2}\sigma_{vn}}$ becomes asymptotically large and causes a corresponding large variance in the retrieve power. However, there are cases of spectrum width values with low SNR that makes $\frac{4}{\mathrm{SNR}} + \frac{2}{\mathrm{SNR}^2}$ larger than $\frac{1}{\pi^{1/2}\sigma_{vn}}$. In these situations, the variance of the retrieved power is caused mainly by the SNR.

[25] **Acknowledgments.** This work is partially supported by the National Severe Storms Laboratory (NOAA/NSSL) under cooperative agreement NA17RJ1227. The authors would like to acknowledge Steven Frasier, F. Lopez-Dekker, and Mike Hoffman for their contribution to the original TEP data.

References

Battan, L. (1973), *Radar Observations of the Atmosphere*, Univ. of Chicago Press, Chicago, Ill.

Capon, J. (1969), High-resolution frequency-wavenumber spectrum analysis, *Proc. IEEE*, *57*(8), 1408–1418.

Cheong, B., M. Hoffman, R. Palmer, S. Frasier, and F. Lopez-Dekker (2006), Phased-array design for biological clutter rejection: Simulation and experimental validation, *J. Atmos. Oceanic Technol.*, *23*(4), 585–598.

Doran, J., J. Fast, and J. Horel (2002), The VTMX 2000 campaign, *Bull. Am. Meteorol. Soc.*, *83*(4), 537–551.

Doviak, R., and D. Zrnić (1993), *Doppler Radar and Weather Observations*, Academic, San Diego, Calif.

Friedrich, K., M. Hagen, and T. Einfalt (2006), A quality control concept for radar reflectivity, polarimetric parameters, and Doppler velocity, *J. Atmos. Oceanic Technol.*, *23*(7), 865–887.

Fukao, S. (2007), Recent advances in atmospheric radar study, *J. Meteorol. Soc. Jpn.*, *85B*, 215–239.

Gordon, W. (1997), An effect of receiver noise on the measurement of Doppler spectral parameters, *Radio Sci.*, *32*(4), 1409–1423.

Harris, F. (1978), On the use of windows for harmonic analysis with the discrete Fourier transform, *Proc. IEEE*, *66*(1), 51–83.

Haykin, S. (1996), *Adaptive Filter Theory*, 3rd ed., Prentice-Hall, Upper Saddle River, N. J.

Hélal, D., M. Crochet, H. Luce, and E. Spano (2009), Radar imaging and high-resolution array processing applied to a classical VHF-ST profiler, *J. Atmos. Sol. Terr. Phys.*, *63*, 263–274.

Hildebrand, P., and R. Sekhon (1974), Objective determination of noise-level in Doppler spectra, *J. Appl. Meteorol.*, *13*(7), 808–811.

Hubbert, J., V. Bringi, and D. Brunkow (2003), Studies of the polarimetric covariance matrix. Part I: Calibration methodology, *J. Atmos. Oceanic Technol.*, *20*(5), 696–706.

Hysell, D. (1996), Radar imaging of equatorial F region irregularities with maximum entropy interformetry, *Radio Sci.*, *31*(6), 1567–1578.

Marple, S. (1987), *Digital Spectral Analysis: With Applications*, Prentice-Hall, Upper Saddle River, N. J.

Mead, J., G. Hopcraft, S. Frasier, B. Pollard, C. Cherry, D. Schaubert, and R. McIntosh (1998), A volume-imaging radar wind profiler for atmospheric boundary layer turbulence studies, *J. Atmos. Oceanic Technol.*, *15*(4), 849–859.

Melnikov, V. (2006), One-lag estimators for cross-polarization measurements, *J. Atmos. Oceanic Technol.*, *23*(7), 915–926.

National Research Council (2002), *Weather Radar Technology Beyond NEXRAD*, Natl. Acad. Press, Washington, D. C.

Palmer, R., M. Larsen, E. Sheppard, S. Fukao, M. Yamamoto, T. Tsuda, and S. Kato (1993), Poststatistic steering wind estimation in the troposphere and lower stratosphere, *Radio Sci.*, *28*(3), 261–272.

Palmer, R., B. Cheong, M. Hoffman, S. Frasier, and F. Lopez-Dekker (2005), Observations of the small-scale variability of precipitation using an imaging radar, *J. Atmos. Oceanic Technol.*, *22*(8), 1122–1137.

Pollard, B., S. Khanna, S. Frasier, J. Wyngarrd, D. Thomson, and R. McIntosh (2000), Local structure of the convective boundary layer from a volume-imaging radar, *J. Atmos. Sci.*, *57*(14), 2281–2296.

Srivastava, R., and A. Jameson (1979), Time-domain computation of mean and variance of Doppler spectra, *J. Appl. Meteorol.*, *18*(2), 189–194.

Stoica, P., and R. Moses (2005), *Spectral Analysis of Signals*, Prentice-Hall, Upper Saddle River, N. J.

Strauch, R., R. Kropfli, W. Sweezy, W. Moninger, and R. Lee (1978), Improved Doppler velocity estimates by the poly-pulse-pair method, paper presented at 18th Conference on Radar Meteorology, Am. Meteorol. Soc., Atlanta, Ga.

Torres, S., and D. Zrnić (2003), Whitening in range to improve weather radar spectral moment estimates. Part I: Formulation and simulation, *J. Atmos. Oceanic Technol.*, *20*(11), 1433–1448.

Yu, T.-Y., R. Palmer, and P. Chilson (2001), An investigation of scattering mechanisms and dynamics in PMSE using coherent radar imaging, *J. Atmos. Sol. Terr. Phys.*, *63*(17), 1797–1810.

Zhang, G., R. Doviak, J. Vivekanandan, W. Brown, and S. Cohn (2004), Performance of correlation estimators for spaced antenna wind measurement in the presence of noise, *Radio Sci.*, *39*, RS3017, doi:10.1029/2003RS003022.

B. L. Cheong, K. D. Le, R. D. Palmer, T.-Y. Yu, and G. Zhang, Atmospheric Radar Research Center, University of Oklahoma, 120 David L. Boren Blvd., Ste. 4610, Norman, OK 73072-7307, USA. (boonleng@ou.edu; khoi@ou.edu; rpalmer@ou.edu; tyu@ou.edu; guzhang1@ou.edu)

S. M. Torres, Cooperative Institute for Mesoscale Meteorological Studies, University of Oklahoma, 120 David L. Boren Blvd., Ste. 4921, Norman, OK 73072-7307, USA. (sebastian.torres@noaa.gov)